MATERIALS SCIENCE

Lead-free (Ag,K)NbO₃ materials for high-performance explosive energy conversion

Zhen Liu^{1,2}, Teng Lu², Fei Xue³, Hengchang Nie¹, Ray Withers², Andrew Studer⁴, Felipe Kremer⁵, Narendirakumar Narayanan^{2,4}, Xianlin Dong^{1,6}, Dehong Yu⁴, Longqing Chen³, Yun Liu²*, Genshui Wang^{1,6}*

Explosive energy conversion materials with extremely rapid response times have broad and growing applications in energy, medical, defense, and mining areas. Research into the underlying mechanisms and the search for new candidate materials in this field are so limited that environment-unfriendly Pb(Zr,Ti)O₃ still dominates after half a century. Here, we report the discovery of a previously undiscovered, lead-free (Ag_{0.935}K_{0.065})NbO₃ material, which possesses a record-high energy storage density of 5.401 J/g, enabling a pulse current ~ 22 A within 1.8 microseconds. It also exhibits excellent temperature stability up to 150°C. Various in situ experimental and theoretical investigations reveal the mechanism underlying this explosive energy conversion can be attributed to a pressure-induced octahedral tilt change from $a^-a^-c^+$ to $a^-a^-c^-/a^-a^-c^+$, in accordance with an irreversible pressure-driven ferroelectricantiferroelectric phase transition. This work provides a high performance alternative to Pb(Zr,Ti)O₃ and also guidance for the further development of new materials and devices for explosive energy conversion.

Copyright © 2020 The Authors, some rights reserved; exclusive licensee American Association for the Advancement of Science. No claim to original U.S. Government Works. Distributed under a Creative Commons Attribution License 4.0 (CC BY).

INTRODUCTION

The intense research interest in the area of energy harvesting and its conversion arises from the ever-increasing global demand for energy. In that area, extremely rapid (or "explosive," "pulse power") energy conversion, a field initiated as a consequence of research into nuclear fusion in the 1950s, has now become a critical technique due to its numerous applications as compact devices in defense, mining, renewable energy, and medical industries [for instance, directed energy, remote power supplies, rapid charging of capacitors, mine detection, propulsion, lightning and electromagnetic pulse simulators, electromagnetic launchers, mineral and oil exploration, blasting operations at mines and quarries, and neutron generator power systems (1, 2)]. Ferroelectric materials are in a critical position in this area because of their unique response to external mechanical stimuli (3–8). For instance, a shock pressure compression can release the bound electric charges of poled ferroelectric (FE) ceramics within a short period of time (~µs), thereby generating a sharp current/voltage pulse with megawatts of electrical power (9). This pressure-driven depolarization behavior in FE materials enables the technologically useful fast conversion of mechanical energy to electrical energy for applications, which have driven extensive research in this field for many years. The pressure-driven FE-antiferroelectric (AFE) phase transition of electroceramics seems to be the most straightforward approach due to the nonpolar nature of the AFE state (10). Most previous work in this area has been devoted to searching for the most promising candidate among lead-based materials, inspired by

To realize novel, lead-free, energy harvesting materials showing a pressure-driven FE-AFE phase transition, it is considered as a prerequisite that these materials should have a small energy barrier between an FE and an AFE state. Besides undergoing a pressuredriven FE-AFE phase transition, promising FE materials should also have a high remnant polarization, P_p to harvest more pulsed electrical power. In this contribution, K-doped AgNbO₃ (AN) is selected to investigate as the AN holding matrix exhibits antiferroelectricity and a large, high–*E*-field-induced polarization ($P \sim 52\mu\text{C/cm}^2$) (15–18). KNbO₃, on the other hand, exhibits an FE phase (19) but can form binary (Ag_{1-x}K_x)NbO₃ (AKN) solid solutions with AN (20). Within these AKN solid solutions, the relative stability of the FE and AFE phase can be modulated through tailoring of the composition to give a material with a high potential to realize a pressure-induced FE-AFE phase transition and potentially be able to serve as an effective alternative to lead-containing materials for energy harvesting and conversion applications. However, neither theoretical nor experimental research has been done to date to investigate the response of AKN and other AN-based FE materials under pressure environments.

In this work, lead-free AKN FE materials are designed and synthesized for explosive energy conversion applications. It is found that AKN ceramics with the composition ($Ag_{0.935}K_{0.065}$)NbO₃ experience an FE-AFE phase transition, leading to a sharply decreased P_r

the outstanding FE properties of $Pb(Zr_{1-x}Ti_x)O_3$ (PZT) and the prototype AFE material $PbZrO_3$. The ~2% Nb-doped $Pb(Zr_{0.95}Ti_{0.05})O_3$, i.e., $Pb_{0.99}(Zr_{0.95}Ti_{0.05})_{0.98}Nb_{0.02}O_3$ (PZT 95/5), was early on recognized to be the best candidate material, as its FE-AFE phase transition could be triggered under a low pressure. For this reason, it has dominated the commercial market for more than half a century (10–14). However, the toxicity of lead and increasing environmental regulation will limit its applications in the future. There is thus an urgent current need for the discovery of lead-free FE materials to replace PZT 95/5. Unfortunately, to the best of our knowledge, no success has been experimentally reported to date that lead-free ferroelectrics can transform to an AFE phase under pressure and thus be an effective lead-free alternative to PZT 95/5 in terms of explosive energy power conversion applications.

¹Key Laboratory of Inorganic Functional Materials and Devices, Shanghai Institute of Ceramics, Chinese Academy of Sciences, 1295 Dingxi Road, Shanghai 200050, China. ²Research School of Chemistry, The Australian National University, Canberra, ACT 2601, Australia. ³Department of Materials Science and Engineering, Pennsylvania State University, University Park, PA 16802, USA. ⁴Australian Nuclear Science and Technology Organisation, Lucas Heights, NSW 2234, Australia. ⁵Centre for Advanced Microscopy, Australian National University, 131 Garran Road, Acton, Canberra, ACT 2601, Australia. ⁶State Key Laboratory of High Performance Ceramics and Superfine Microstructure, Shanghai Institute of Ceramics, Chinese Academy of Sciences, 1295 Dingxi Road, Shanghai 200050, China.

^{*}Corresponding author. Email: genshuiwang@mail.sic.ac.cn (G.W.); yun.liu@anu. edu.au (Y.L.)

as the hydrostatic pressure increases to around 300 MPa. This is quite intriguing because the pressure-driven FE-AFE phase transition has never been experimentally observed in lead-free ferroelectrics previously. An in situ neutron diffraction technique and phenomenological theory are used to elucidate how the structure of this material evolves under hydrostatic pressure. A device has also been designed and fabricated using this AKN material and a high electrical current pulse output of 22 A achieved, as demonstrated in shock-wave compression experiments. In addition, the energy storage density and temperature stability of this new, lead-free $(Ag_{0.935}K_{0.065})NbO_3$ ceramic material are found to be substantially higher/better than those of the classical, lead-containing PZT 95/5 ceramic material, further facilitating the possible substitution of PZT 95/5 by $(Ag_{0.935}K_{0.065})$ NbO3 in explosive energy conversion applications.

RESULTS

The AKN ceramics have a dense microstructure with low porosity and grain sizes varying from 1 to 10 µm, as is apparent from the scanning electron micrograph image in fig. S1. Figure 1A shows the pressure-dependent polarization-electric field (P-E) loops of (Ag_{0.935}K_{0.065})NbO₃ ceramics measured under a 1-Hz electrical sine waveform at room temperature. The (Ag_{0.935}K_{0.065})NbO₃ material displays a typical single loop–featured FE character with a high P_r of 33 μ C/cm² at ambient pressure, while a well-developed, double *P-E* loop-featured, AFE hysteresis behavior is observed at 350 MPa with a notably decreased P_r of 8 μ C/cm². This suggests that the AFE phase has been successfully induced out of the initial FE phase by the applied pressure. A detailed evolution of the P-E loops of (Ag_{0.935}K_{0.065})NbO₃ ceramics with increasing hydrostatic pressure is presented in fig. S2. It can be seen that the FE phase of the (Ag_{0.935}K_{0.065})NbO₃ materials gradually changes to an AFE phase with increasing hydrostatic pressure of up to ~300 MPa. Note that the location of $(Ag_{0.935}K_{0.065})NbO_3$ is near the compositional FE-AFE phase boundary according to a previous study (20). For comparison purposes, another $(Ag_{1-x}K_x)NbO_3$ composition $(Ag_{0.94}K_{0.06})$ NbO₃, also located near this FE-AFE phase boundary, was also prepared. Its pressure-dependent electrical properties are shown in fig. S3. The initial state of (Ag_{0.94}K_{0.06})NbO₃ shows a pinched P-E hysteresis loop and its P_r displays a sudden drop when the pressure surpasses 150 MPa. However, although its dynamic response to an E-field suggests a nonzero P_r , the zero piezo-response ($d_{33} = 0$) of (Ag_{0.94}K_{0.06})NbO₃ after poling indicates that this composition is not suited to store energy.

To evaluate its in situ depolarization behavior under pressure, the (Ag_{0.935}K_{0.065})NbO₃ ceramics were poled in silicone oil under an *E*-field of 4 kV/mm for 10 min at room temperature (average d_{33} = 49 pC/N) and then placed in an oil hydrostatic pressure environment at room temperature. As the pressure increased, the released electric current was synchronously collected during the depolarization process and then integrated to obtain an estimate of remnant polarization as a function of applied pressure. Figure 1B shows the in situ depolarization curve of prepoled (Ag_{0.935}K_{0.065})NbO₃ FE ceramics with increasing hydrostatic pressure at room temperature. It is found that at up to 240 MPa, the remnant polarization remains almost unchanged at around 33 μ C/cm². Over this pressure range, the depolarization current is dominated by electromechanical coupling effects such as the piezoelectric effect, and therefore, only a small depolarization current is produced. By contrast, when the

pressure increases up to 300 MPa, the pressure-driven FE-AFE phase transition occurs, and most of the bound screening charges stored in the prepoled (Ag_{0.935}K_{0.065})NbO₃ sample are sharply released over a narrow pressure range. In this case, it is found that around 23 $\mu\text{C/cm}^2$ was released when the hydrostatic pressure was increased from 290 to 330 MPa. This is in good agreement with the pressure-dependent *P-E* measurements.

Figure 1 (C and D) shows the hydrostatic pressure–dependent, dielectric constant and dielectric loss of a poled, (Ag_{0.935}K_{0.065}) NbO₃ FE ceramic at room temperature. Upon increasing the pressure to ~300 MPa, both the dielectric constant and loss show abrupt anomaly changes, in accordance with a pressure-induced FE-AFE phase transition. During the process of the pressure withdrawal, however, no sudden change happens, strongly suggesting that the pressure-driven FE-AFE transition is irreversible. The dielectric constant of fresh (Ag_{0.935}K_{0.065})NbO₃ ceramics is measured to be ~500, reducing to 295 after poling, and lastly to 236 after the application and withdrawal of 430-MPa hydrostatic pressure. This large difference between the measured dielectric constant again indicates that the (Ag_{0.935}K_{0.065})NbO₃ sample does not revert back to its initial fresh polarization state after completing the pressure-induced FE-AFE phase transition process, with its dielectric constant being 45% less than that of the fresh sample, although the remnant polarization of both states is near zero.

To evaluate the real performance of $(Ag_{0.935}K_{0.065})NbO_3$ materials for explosive energy conversion applications, the dynamic discharge response of the resultant AKN FE capacitor devices was then measured (Fig. 1E). It can be seen that a well-developed electrical square current curve is achieved when a 6.9-GPa external shock pressure is applied and a 120-ohm external resistor is used. The generated pulse current peak value can be as high as 22 A. The released charge density under shock pressure reaches 38 $\mu\text{C/cm}^2$, while the dynamic discharging process is completed within 1.8 μs , comparable to that of PZT 95/5 but with the distinct advantage of being lead free, i.e., nonharmful to the environment. Moreover, the bulk density of $(Ag_{0.935}K_{0.065})\text{NbO}_3$ ceramics (~6.4 g/cm³) is much lighter than that of the PZT 95/5 material (~7.9 g/cm³) (21), which is also a notable advantage due to a worldwide demand for electrical device miniaturization and reduction in weight.

The energy storage density per unit of weight in FE materials can be calculated theoretically via the following equation: W = $P_r^2/2(\varepsilon_0^*\varepsilon_r^*\rho)$, where ρ is the bulk density of the FE ceramics and ε_r represents the relative dielectric constant of the depoled AFE phase (2). When calculating the energy storage density, the stress-induced released charge density, which represents the real charge density that can be achieved from the shock-wave experiments, should be used as the value of P_r . Figure 1F gives a comparison of the calculated energy storage density of (Ag_{0.935}K_{0.065})NbO₃ with other reported FE materials (9, 22, 23). It is evident that the $(Ag_{0.935}K_{0.065})NbO_3$ FE ceramics show a record-high energy storage density of 5.401 J/g, substantially higher than that of the current commercially used PZT 95/5 ceramics (2.929 J/g). The energy storage density per unit of volume is also calculated via the equation: $W = P_r^2/2(\varepsilon_0 * \varepsilon_r)$. The result is listed in table S1, together with other reported materials. It can be seen that with regard to the energy density per unit of volume, (Ag_{0.935}K_{0.065})NbO₃ is also the highest reported among PZT 95/5 and other FE materials, with a record-high value of 34.57 J/cm³. The higher energy density is largely due to the larger remnant polarization, lower bulk density, and smaller dielectric constant of the (Ag_{0.935}K_{0.065})NbO₃ ceramics.

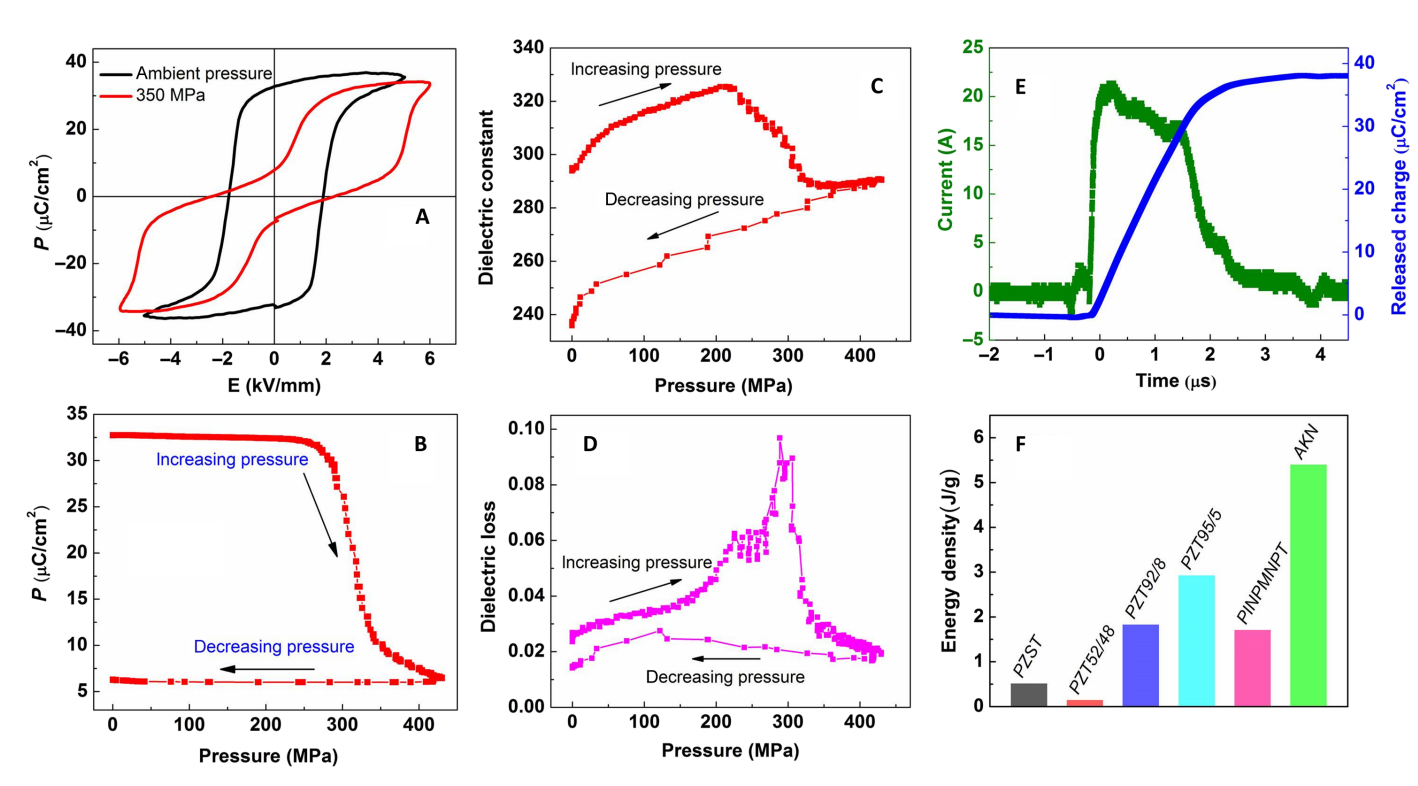


Fig. 1. Macroscopic performance of $(Ag_{0.935}K_{0.065})NbO_3$ FE ceramics and devices. (A) The pressure-dependent polarization—electric field (P-E) loops of $(Ag_{0.935}K_{0.065})NbO_3$ FE ceramics measured at room temperature and 1 Hz. (B) The in situ depolarization curve of prepoled $(Ag_{0.935}K_{0.065})NbO_3$ FE ceramics under gradually increasing hydrostatic pressures at room temperature. The data were collected during the pressure-driven depolarization process and then integrated to obtain the pressure-dependent polarization. (C and D) The hydrostatic pressure-dependent dielectric constant and dielectric loss of poled $(Ag_{0.935}K_{0.065})NbO_3$ FE ceramics at room temperature. (E) Practical dynamic discharging response of assembled $(Ag_{0.935}K_{0.065})NbO_3$ FE ceramic devices collected under shock pressure of 6.9 GPa. (F) A comparison of the energy storage densities per unit of weight of the $(Ag_{0.935}K_{0.065})NbO_3$ ceramics and other FE materials.

Their temperature stability, reflecting the working endurance to environmental conditions, is also a critical factor for material selection and device design. Figure S4A shows the dielectric constant of the poled (Ag_{0.935}K_{0.065})NbO₃ FE ceramics as a function of temperature from room temperature to 400°C at different frequencies. It can be seen that the (Ag_{0.935}K_{0.065})NbO₃ ceramics experience no disruptive phase transition until the temperature rises to 150°C, when an abrupt step-like increment of the dielectric constant emerges, which can be ascribed to an FE-FE phase transition. Figure S4B displays the evolution of the P-E loops of the (Ag_{0.935}K_{0.065})NbO₃ ceramics with increasing temperature from room temperature up to 180°C. With increasing temperature to 150°C, the coercive electric field decreases, but the important large remnant polarization remains essentially unchanged, indicating excellent, temperature-independent FE properties. The thermal depolarization evolution of the $(Ag_{0.935}K_{0.065})$ NbO₃ ceramics was therefore examined (see fig. S4C). A sharp, thermal depolarization peak at 150°C can be observed because of the FE-FE phase transition, further supporting the material's remarkable temperature stability. This is an advantage over the current commercially used PZT 95/5 ceramics where a similar low-temperature FE-to-high-temperature FE phase transition leads to a loss of more than 10% of its polarization at a significantly lower temperature, 41 to 70°C (2, 24). Moreover, the Curie temperature (T_C) of $(Ag_{0.935}K_{0.065})$ NbO₃ (250°C) is also marginally higher than that of PZT 95/5 (227°C), adding to its superiority with regard to temperature stability (2). This advantage is quite important for the practical application of (Ag_{0.935}K_{0.065})NbO₃ materials, since it is always necessary for FE devices

to operate under different temperature environments, and the fabrication of FE devices always involves a higher-temperature sealing process. It also needs to be stressed that the $(Ag_{0.935}K_{0.065})NbO_3$ material reported here is the first experimentally demonstrated, lead-free FE material that undergoes a substantial pressure-driven FE-AFE phase transition. A careful study on the structure and phase transition and their interactions with the pressure-driven properties of this material is important to enhance the understanding of this $(Ag_{0.935}K_{0.065})NbO_3$ material and thus provide new insight into the further development of lead-free materials for pressure applications.

DISCUSSION

Figure 2 (A and B) shows typical selected-area electron diffraction patterns (SAEDPs) of $(Ag_{0.935}K_{0.065})$ NbO $_3$ ceramic powders collected along (i) $[001] = [0-11]_p$ and (ii) $[0-13] = [0-21]_p$ zone axes, respectively. The SAEDPs were first indexed with reference to a pseudo-cubic (Pm-3m) parent perovskite structure (subscript p). In addition to the well-defined set of parent perovskite Bragg reflections (labeled **G** hereafter), the $\mathbf{G} \pm \frac{1}{2}(100)_p$, $\mathbf{G} \pm \frac{1}{2}(011)_p$, and $\mathbf{G} \pm \frac{1}{2}(111)_p$ satellite reflections are also clearly present. As the doping level of K is only 6.5%, the appearance of satellite reflections is unlikely to be linked to cation ordering. The relatively intense $\frac{1}{2}(100)_p$ reflection indicates that the FE structure of $(Ag_{0.935}K_{0.065})$ NbO $_3$ has a doubled lattice parameter, i.e., $\mathbf{a} = 2\mathbf{a}_p$ with respect to the parent perovskite structure. The unambiguous FE properties exclude a supercell induced by antiparallel displacements, which often exist in AFE materials.

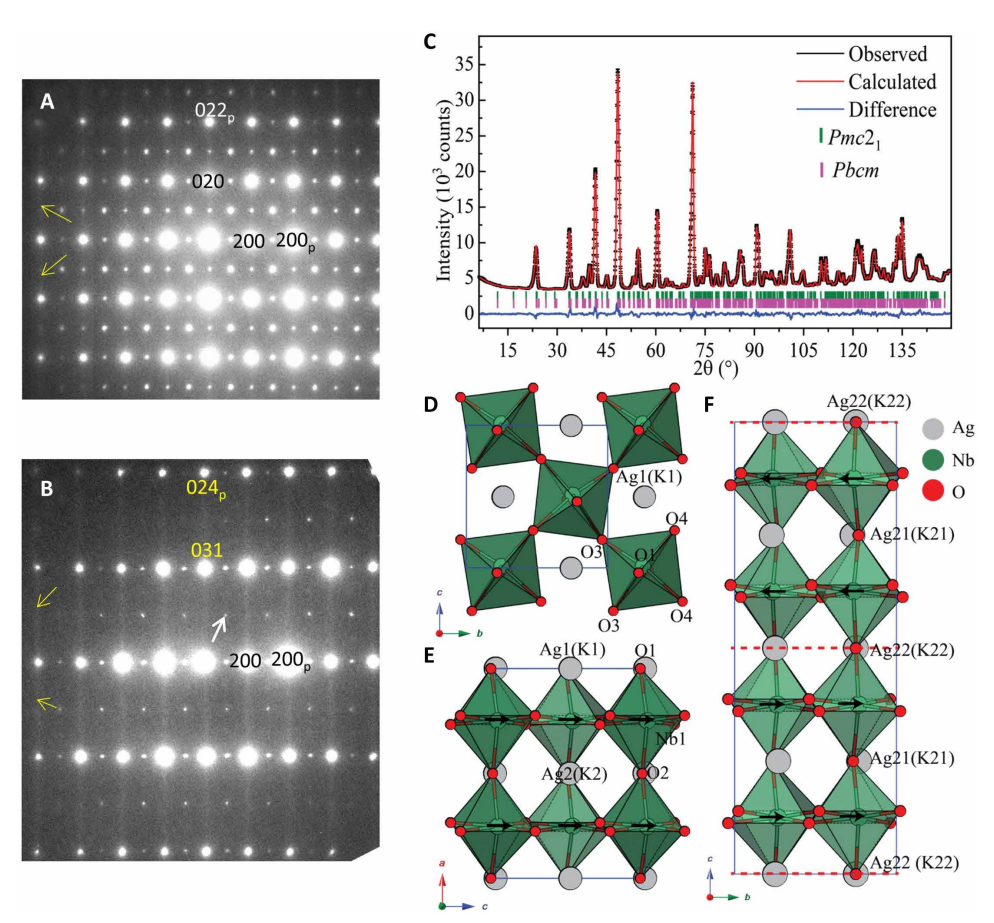


Fig. 2. Structural analysis of (Ag_{0.935}K_{0.065})**NbO**₃ **ceramics.** Selected-area electron diffraction patterns (SAEDPs) of a crushed fragment of an (Ag_{0.935}K_{0.065})NbO₃ ceramic along (**A**) [001] = $[0-11]_p$ and (**B**) $[0-13] = [0-21]_p$ zone axis directions. The very weak, arrowed in white, reflections [in (B)] arise from a small amount of a second twin domain. (**C**) The Rietveld refinement of the NDP of (Ag_{0.935}K_{0.065})NbO₃ powders in terms of a two-phase model ($Pmc2_1 + Pbcm$). The refined $Pmc2_1$ phase structure viewed along (**D**) the a axis and (**E**) the b axis. (**F**) The refined Pbcm phase structure viewed along its a axis.

Thus, octahedral tilting is proposed to be the main reason for the existence of the obtained satellite reflections. With respect to the octahedral tilting, the simultaneous observation of $G \pm \frac{1}{2}(111)_p$ and $G \pm \frac{1}{2}(110)_p$ satellite reflections suggests the coexistence of both inand antiphase tilting, which can be expressed as either $a^-a^-c^+$ or $a^0b^-c^+$ in Glazer notation (25). The corresponding distorted structures induced by such octahedral tilting can thus be assigned to either Pbnm $(c\equiv 2c_p, a\equiv a_p + b_p, and b\equiv a_p - b_p)$ or Cmcm $(c\equiv 2c_p, a\equiv 2a_p, a\equiv 2a_$ and $b\equiv 2b_p$) space groups, respectively. Intriguingly, the AFE structure of pure AgNbO₃ with *Pbcm* symmetry has an unusual $a^-a^-c^+/a^-a^-c^$ octahedral tilting system (see Fig. 2F above), indicating alternative in- and antiphase octahedral tilting around the c axis (equivalent [001]_p direction) (26–28). As adjacent NbO₆ octahedra present in-phase tilting as one unit, the tilting system of this half of the AgNbO₃ unit cell is in accordance with an $a^-a^-c^+$ tilting system, which can reproduce the diffraction patterns shown in Fig. 2 (A and B) (29).

However, the appearance of ferroelectricity also requires the condensation of a zone center mode, i.e., the resultant symmetry should be a subgroup of either *Pbnm* or *Cmcm*. Upon further investigating their isotropy subgroups (30), it is found that spontaneous polarization can develop in either the $[001]_p$ direction or the $[110]_p$ direction. The dipole moments within the average structure of the two end

members, namely, AgNbO₃ and KNbO₃ are all aligned along [110]_p (31), which convinces us that in $(Ag_{0.935}K_{0.065})NbO_3$, the spontaneous polarization should also develop along the [110]_p direction (28). Constrained by the direction of the polar axis, the resultant subgroup of *Pbnm* is thus assigned to $Pmc2_1$ ($\mathbf{a} \equiv 2\mathbf{a}_p$, $\mathbf{b} \equiv \mathbf{b}_p + \mathbf{c}_p$ and $\mathbf{c} \equiv -\mathbf{b}_p + \mathbf{c}_p$), while no suitable subgroup could be determined for *Cmcm* symmetry. The proposed FE structure for (Ag_{0.935}K_{0.065})NbO₃ is similar to the noncentrosymmetric space group obtained in NaNbO₃ (32). By adopting this polar structure, it is found the simulated patterns at the same zone axes (fig. S5) reproduce almost all features observed in the SAEDPs. However, the tiny peaks shown in Fig. 2B, indicated by the white arrows, are unobservable in the simulated pattern and can be shown to originate from a small amount of a second domain within the illuminated area required to take the SAEDP. In addition to the lattice reflections, it is evident that sharp diffuse streaking (indicated by the yellow arrows) in Fig. 2 (A and B) runs along the [020]* and [031]* reflections perpendicular to the a direction through all the parent Bragg reflections, confirming the nature of these G ± (100)_p* sheets of diffuse intensity. This kind of diffuse scattering, which is well documented in AFE AgNbO₃, FE KNbO₃, and FE BaTiO₃ (28, 33, 34), originates from one-dimensional polar chains along the [100] direction in real space, reflecting the local disordered nature of the Nb⁵⁺ ions.

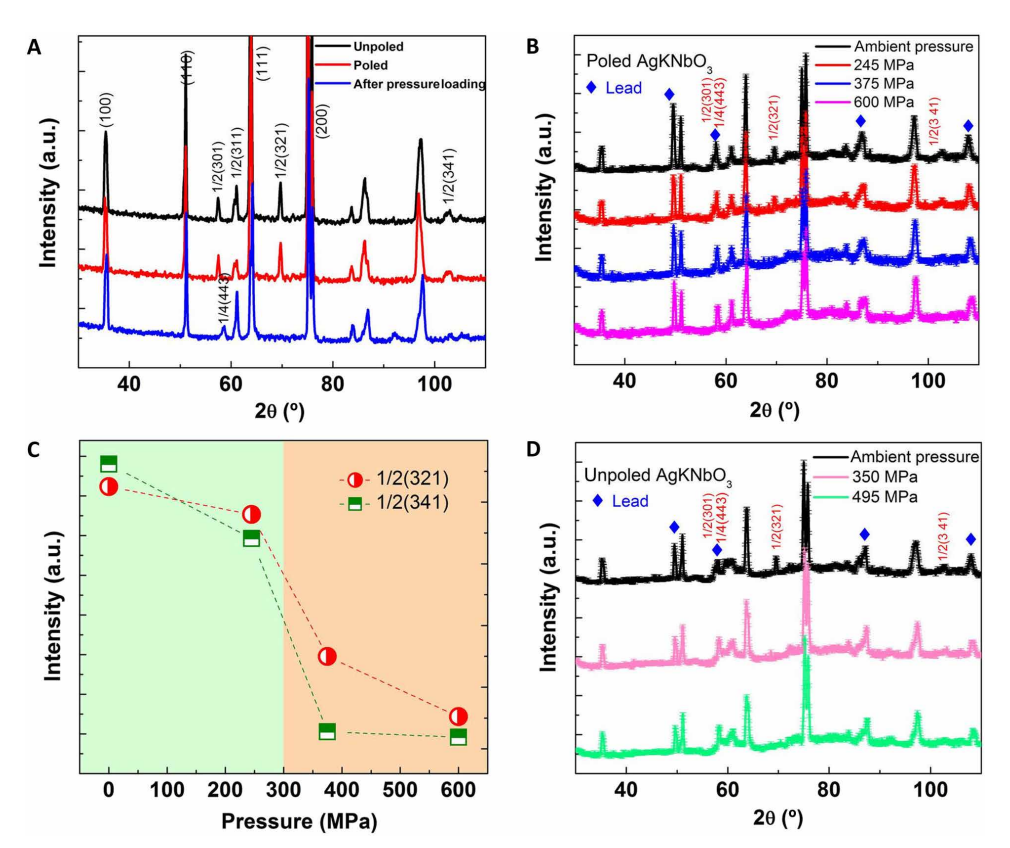


Fig. 3. In situ NDPs of (Ag_{0.935}K_{0.065})NbO₃ ceramics. (A) NDPs of an unpoled (fresh) (Ag_{0.935}K_{0.065})NbO₃ ceramic sample, a poled (Ag_{0.935}K_{0.065})NbO₃ ceramic sample, and a poled (Ag_{0.935}K_{0.065})NbO₃ ceramic after experiencing 600-MPa hydrostatic pressure. (B) In situ NDPs of poled (Ag_{0.935}K_{0.065})NbO₃ ceramics as a function of increasing hydrostatic pressure. (C) The integrated area values of the 1/2(321) and 1/2(341) peaks from NDP data for poled (Ag_{0.935}K_{0.065})NbO₃ samples as a function of hydrostatic pressure. (D) In situ NDPs of unpoled (Ag_{0.935}K_{0.065})NbO₃ ceramics with increasing hydrostatic pressure. For the in situ NDP measurements, lead shards, whose lattice parameter is already known as a relation of hydrostatic pressure, were used to calibrate the pressure applied onto the (Ag_{0.935}K_{0.065})NbO₃ ceramics. a.u., arbitrary units.

To further confirm the proposed structural model, Rietveld refinement was conducted on the neutron diffraction pattern (NDP) of the $(Ag_{0.935}K_{0.065})NbO_3$ powders. Although the proposed singlephase Pmc2₁ structure could predict most of the observed peaks (fig. S6), some reflections (enlarged in fig. S6, B and C) are heavily underestimated. The appearance of underestimated 1/4(443)_p and ¹/₄(229)_p peaks is consistent with the pure AFE AgNbO₃-type structure with Pbcm symmetry (28). Figure 2C shows a Rietveld refinement of the NDP data of the (Ag_{0.935}K_{0.065})NbO₃ powders based on a twophase $(Pmc2_1 + Pbcm)$ model. Note that the fitting to the experimental data is notably improved, compared with that in fig. S6. The refined *Pmc2*₁ and *Pbcm* phase structures are shown in Fig. 2 (D to F). The details regarding lattice parameters, phase fractions, atomic coordinates, and refinement reliability factors are listed in the Supplementary Materials. As illustrated in Fig. 2E, the Nb⁵⁺ ion displaces ~0.08 Å along the c direction from its undistorted position, while the apical oxygens, $O1^{2-}$ and $O2^{2-}$ ions, shift along the +c direction. These offcenter displacements lead to a spontaneous polarization along the c direction. Intriguingly, as mentioned previously, the structure of the FE Pmc2₁ phase is similar to one unit, i.e., two adjacent octahedral layers delineated by the dashed red lines shown in Fig. 2F, of the AFE *Pbcm* phase, where the dashed red lines indicate the antiphase boundaries between these units. The coexistence of Pmc21 and Pbcm phases suggests a very low energy barrier between the FE and AFE structures, consistent with the observed properties characterization. It is also found that the calculated cell volume (one parent perovskite unit) of the $Pmc2_1$ phase (61.3 Å³) is slightly larger than that of the Pbcm phase (61.1 Å³), supporting the fact that pressure stabilizes the AFE phase.

The above NDP results indicate that the most easily observable differences between the AFE and the FE phase reside in differences in octahedral tilting and the associated characteristic satellite reflections. As shown in the top NDP of Fig. 3A (for the unpoled ceramic sample), for example, it is clear that characteristic FE phase reflections arising from $a^-a^-c^+$ octahedral tilting, i.e., $\frac{1}{2}(301)_p$, $\frac{1}{2}(311)_p$, $\frac{1}{2}(321)_p$, and ½(341)_p reflections, are clearly observed, while no trace of the characteristic satellite reflections associated with the $a^-a^-c^-/a^-a^-c^+$ tilt system and the AFE phase, such as ¼(443)_p and ¼(229)_p (see, e.g., the bottom NDP of Fig. 3A), is observed. Evidently, NDPs of both the poled and unpoled ceramic samples initially contain only a pure FE phase, which seems, at first glance, to be inconsistent with the Rietveld refinement results described above using powder samples. However, when the bulk ceramic sample was ground into a powder, residual stress was unavoidably induced, and the differences between NDPs measured for bulk ceramics and powder samples suggest a high sensitivity of (Ag_{0.935}K_{0.065})NbO₃ to external mechanical processing. The bottom NDP of Fig. 3A gives the pattern for poled ceramic samples after the application, and following the withdrawal, of 600-MPa hydrostatic pressure. For this sample, the initial FE phase has clearly transformed into the AFE phase as evidenced by the appearance of the $\frac{1}{4}(443)_p$ and $\frac{1}{4}(229)_p$ reflections and associated disappearance of the $\frac{1}{2}(301)_p$, $\frac{1}{2}(321)_p$, and $\frac{1}{2}(341)_p$ reflections. This confirms that applied pressure can indeed induce the transition of $(Ag_{0.935}K_{0.065})$ NbO₃ samples from an initial FE *Pmc*2₁ phase to an AFE *Pbcm* phase.

An in situ, neutron diffraction experiment under hydrostatic pressure of the poled (Ag_{0.935}K_{0.065})NbO₃ ceramic samples was then conducted to illustrate the pressure-induced phase transition process. Figure 3B shows NDPs of the poled (Ag_{0.935}K_{0.065})NbO₃ ceramics under ambient pressure and hydrostatic pressures of 245, 375, and 600 MPa, respectively, as calculated from the marked peak shifts of the lead standard. Because of the influence of the fluorinert and the pressure cell environment, the quality of patterns is not as good as those taken without pressure cells. Nonetheless, unambiguous changes in the observed characteristic satellite reflections with increasing pressure are still observable. The patterns at ambient pressure and 245 MPa, for example, show the clear presence of ½(321)_n and ½(341)_p superlattice peaks, while the same superlattice reflections disappeared when the pressure was increased to 375 and 600 MPa. Although the ½(301)_p and ¼(443)_p superlattice reflections overlap with a peak from the lead shards, we can still in situ observe the pressure-driven FE-AFE phase transition in this poled (Ag_{0.935}K_{0.065}) NbO₃ sample. Figure 3C shows the integrated intensities of the $\frac{1}{2}(321)_p$ and $\frac{1}{2}(341)_p$ satellite peaks as a function of hydrostatic pressure. As aforementioned, the intensities of these satellite reflections can be considered to be a good indicator of the presence of the FE phase. Their sharp decrease in intensity over the pressure range from 245 to 375 MPa proves that the pressure-driven FE-AFE phase transition occurs at around 300 MPa, consistent with the macroscopic property measurements. In situ NDPs under pressure were also taken from an unpoled (Ag_{0.935}K_{0.065})NbO₃ sample (Fig. 3D) to illustrate whether the pressure-driven phase transition is inherent or just characteristic of the poled ceramics. It is found that the same evolution trend was seen for the unpoled samples as for the poled samples. This provides strong evidence that (Ag_{0.935}K_{0.065})NbO₃ samples do indeed undergo an FE-AFE phase transition under pressure conditions no matter whether they were prepoled or not. Moreover, from the NDP data collected after withdrawal of the pressure (Fig. 3A), it can also be inferred that the (Ag_{0.935}K_{0.065})NbO₃ ceramics remain in the AFE state and do not revert back to the initial FE phase even when the sample environment reverses back to ambient pressure. This result shows that the pressure-induced FE-AFE transition is irreversible, again consistent with the dielectric properties behavior shown in Fig. 1 (C and D).

We also use a phenomenological theory to rationalize the pressure effect on the relative stabilities of the FE and AFE phases. We introduce two sets of order parameters: polarization p_i (i = 1 to 3) and q_i (i = 1 to 3) to describe the FE and AFE phases, respectively (35). The model details used are given in the method section. A pressure-composition phase diagram for AKN is then calculated on the basis of energy minimization. As shown in Fig. 4A, K doping favors the FE phase, while hydrostatic pressure favors the AFE phase. Thus, applying pressure can induce the AFE phase, resulting in a depolarization effect. The energy contours with respect to the values of p_1 and p_2 near the FE-AFE phase boundary are plotted in Fig. 4B. The energy minimum at p_1 , $p_2 = 0$ indicates the stable AFE phase, while the local energy minima at the four corners suggest the metastable FE states. Upon increasing the K-doping level sufficiently, the energy wells associated with the FE phase become ever deeper, until the sample becomes FE under ambient conditions.

Figure 4C shows the energy profiles of $(Ag_{0.935}K_{0.065})NbO_3$ (AKN-0.065) and $(Ag_{0.92}K_{0.08})NbO_3$ (AKN-0.08) under different hydrostatic pressures. In the AKN system, although pressure suppresses the stabilities of both the FE and AFE phases, the FE phase is more sensitive to the applied pressure, and the free energy of the FE phase increased more under a certain pressure. Moreover, for AKN-0.065, the difference between the energy minima of the FE and AFE phases under ambient pressure is small, which shows good consistency with the structural analysis. While for AKN-0.08, the difference between the energy minima of the FE and AFE phases under ambient pressure is increased. Thus, it is more difficult to drive the FE-AFE phase transition for AKN-0.08 under higher pressure conditions, as indicated by the energy profiles under 400 MPa in Fig. 4C.

We therefore prepared AKN-0.08 ceramics to experimentally demonstrate the calculation results. Figure 4D shows the *P-E* loops of AKN-0.08 ceramics under ambient pressure and hydrostatic pressures of 400 MPa, respectively. The AKN-0.08 ceramics show strong FE properties, and no abrupt polarization drop is observed although the pressure increases up to 400 MPa. This suggests that a high K-doping level stabilizes the FE phase, and a much higher pressure is needed to trigger the FE-AFE phase transition of AKN-0.08, showing good agreement with the theoretical results. It can therefore be concluded that an FE-AFE phase transition, accompanied by a large polarization change, can be driven by moderate pressure only for AKN-0.065 ceramics, which enables this material to have an excellent fast energy-releasing behavior, driven by pressure or mechanical force.

In summary, a lead-free, high-performance (Ag_{0.935}K_{0.065})NbO₃, FE material has been discovered that shows outstanding potential for next-generation explosive energy conversion applications. This AKN material is the first reported lead-free FE material, which can be experimentally shown to undergo an FE-AFE phase transition upon the application of pressure. Electron diffraction and in situ neutron diffraction analyses have been used to decode the FE-AFE phase transition process, which is shown to be associated with a pressure-driven irreversible change from a *Pmc*2₁, FE phase to a *Pbcm*, AFE phase with the accompanying oxygen octahedral tilt system changing from $a^-a^-c^+$ to $a^-a^-c^-/a^-a^-c^+$. Moreover, a proposed phenomenological theory has been used to further confirm our experimental results. On the basis of these AKN materials, we have successfully manufactured an AKN FE energy storage device, which shows comparable dynamic charge-releasing performance as the current commercially used PZT 95/5 materials. We are convinced that the results presented in this work open up important new research directions in lead-free FE materials and, in particular, to the future search for new lead-free materials for explosive energy conversion applications.

MATERIALS AND METHODS

Sample preparation

The AKN ceramics were synthesized using the traditional solid-state reaction method (36). Ag₂O (\geq 99.7%), Nb₂O₅ (\geq 99.93%), and K₂CO₃ (\geq 99.9%) were used as raw materials. The mixed starting materials were first ball milled in ethanol for 12 hours. The dried powders were then calcined at 870°C for 3 hours in an O₂ atmosphere. After calcination, the powder was ball milled again for 12 hours and pressed into pellets with a diameter of 15 mm using polyvinylalcohol

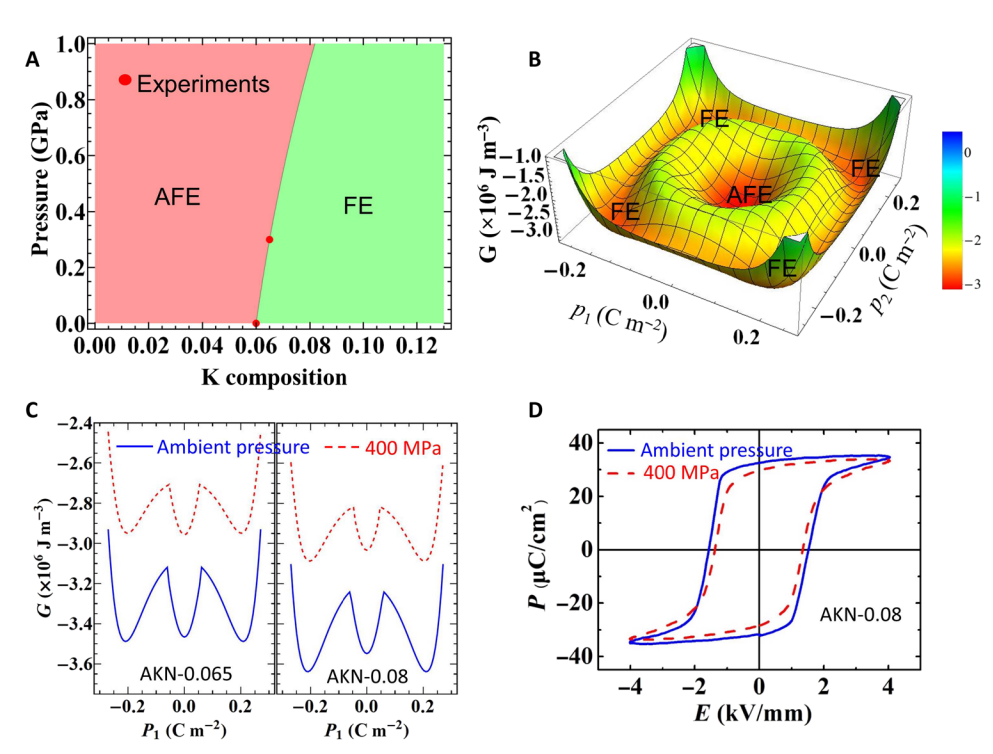


Fig. 4. Phenomenological modeling of the FE and AFE phases. (A) Pressure-composition phase diagram of the $(Ag_{0.935}K_{0.065})NbO_3$ system. (B) Energy contours as a function of p1 and p2 near the FE/AFE phase boundary. The value of p3 is zero, with polarization along the $[110]_p$ direction. (C) The energy profiles of AKN-0.065, i.e., $(Ag_{0.935}K_{0.065})NbO_3$, and AKN-0.08, i.e., $(Ag_{0.92}K_{0.08})NbO_3$ under different hydrostatic pressures. (D) The P-E loops of AKN-0.08 under different hydrostatic pressures.

as a binder. The pellets were then sintered at 1100° C for 3 hours. To prevent the decomposition of silver oxide at higher temperatures, a flowing O_2 atmosphere was used during the sintering process. The obtained ceramics were then polished to 0.5 mm in thickness and 8.0 mm in diameter. For electrical property measurements, silver electrodes were pasted on both sides of the ceramics and sintered at 700° C for 0.5 hours.

Dielectric measurements

The temperature and pressure dependence of the dielectric constant and dielectric loss were measured using a Hewlett Packard LCR meter (1-3-2, Murotanim Nishi-ku, Kobe-shi, Hyogo 651-22, Japan). The hydrostatic pressure environment was generated in a custom-built experimental setup for electrical testing under pressure conditions. Benzyl-toluene was used as the hydrostatic pressure transporting liquid medium. The AKN sample was electrically connected with an integrating capacitor and an electrometer. When starting the controlling unit, a hydrostatic pressure loading setup will operate, and the pressure will thus increase around the sample via the transporting liquid medium and is monitored by pressure monitor. The different data were collected using an A/D conversion card during the pressure-driven depolarization process.

Ferroelectric measurements

The *P-E* loops were characterized at 1-Hz frequency using an aixACCT TF 2000 analyzer FE measuring system (aixACCT Co., Aachen, Germany) using a sinusoidal waveform. The hydrostatic pressure environment was provided using the same setup as described above.

Transmission electron microscopy

The electron diffraction patterns were obtained using a JOEL 2100F FEGTEM instrument.

Scanning electron microscopy

The microstructure of the as-sintered ceramic samples was examined using field-emission scanning electron microscopy (S-4800, Hitachi, Tokyo, Japan).

Neutron scattering

For structural refinement, high-resolution neutron scattering using the Echidna instrument from the Australian Nuclear Science and Technology Organisation (ANSTO) was performed. For neutron analysis under pressure, in situ high-intensity neutron scattering was conducted using the Wombat instrument from ANSTO. A Paris-Edinburgh high-pressure cell was used as the pressure source and pressure holder. Fluorinert was used as the pressure transmission medium to produce the desired hydrostatic pressure environment. Lead shards, whose lattice parameter evolution under pressure variation is already known, were used as filling calibrants to calculate the real pressure value that was applied on the AKN samples when collecting diffraction patterns. A long enough collecting time for each pattern (2 hours) was used to enhance the pattern quality as a result of the weakened intensities of the sample reflections due to the diffraction attenuation arising from the filling fluorinert and the lead shards.

Device demonstration

The shock-wave compression experiment was conducted on a ϕ 57-mm one-stage gas gun facility. The normal mode with the remnant

polarization direction perpendicular to the shock direction was used (12). The specimens embedded within epoxy resin are fixed on the target chamber. The copper flyers were used with different shock speeds to obtain different pressures. A multichannel oscilloscope is used for recording the depoling current signals with a current viewing resistor of 1 ohm. The schematic configuration of the shock-wave load experiment and the equivalent circuit are illustrated in fig. S7. The output circuit is connected to large impedance loads to obtain a high voltage across the FE ceramics. In our experiments, the thickness of the copper flyer is 6 mm. The geometry of the specimens is $16 \times 8 \times 2$ mm. The value of applied shock stress is calculated from impedance matching.

Theory modeling

The total free-energy density is expressed by

$$f = a_{ij}p_{i}p_{j} + a_{ijkl}p_{i}p_{j}p_{k}p_{l} + a_{ijklmn}p_{i}p_{j}p_{k}p_{l}p_{m}p_{n} +$$

$$a_{ijklmnuv}p_{i}p_{j}p_{k}p_{l}p_{m}p_{n}p_{u}p_{v} + b_{ij}q_{i}q_{j} + b_{ijkl}q_{i}q_{j}q_{k}q_{l} +$$

$$b_{ijklmn}q_{i}q_{j}q_{k}q_{l}q_{m}q_{n} + t_{ijkl}p_{i}p_{j}q_{k}q_{l} + \frac{1}{2}s_{ijkl}\sigma_{ij}\sigma_{kl} -$$

$$Q_{ijkl}p_{i}p_{j}\sigma_{kl} - \Lambda_{ijkl}q_{i}q_{j}\sigma_{kl}$$

$$(1)$$

Where a_{ij} , a_{ijkln} $a_{ijklmnuv}$, b_{ij} , b_{ijkl} , b_{ijklmn} , and t_{ijkl} are the coefficients of the Landau polynomial, s_{ijkl} is the compliance tensor, σ_{ij} is the stress tensor, and Q_{ijkl} and Λ_{ijkl} are the FE and AFE electrostrictive coefficients, respectively. The Einstein summation convention is used. Among the coefficients in Eq. 1, we assume that a_{ij} , a_{ijkl} , a_{ijklmn} , $a_{ijklmnuv}$, and b_{ij} are linearly dependent on composition, e.g., $a_{11}(x) = 2(1-x)$ $a_{11}(K_{0.5}Ag_{0.5}NbO_3) + (2x-1)a_{11}(KNbO_3)$, and $b_{11} = b_0[T-T_{q0}(1-c_qx)]$, where x denotes the K composition, b_0 and cq are constants, and $T_{q0}(x)$ is the AFE Curie temperatures of pure AgNbO₃, respectively. The values of a_{ij} , a_{ijkl} , a_{ijklmn} , and $a_{ijklmnuv}$ are taken from $K_{0.5}$ Na_{0.5} NbO₃ and KNbO₃ (37). The other coefficients are fitted on the basis of experimental data, and all the coefficients are given in table S4.

SUPPLEMENTARY MATERIALS

Supplementary material for this article is available at http://advances.sciencemag.org/cgi/content/full/6/21/eaba0367/DC1

REFERENCES AND NOTES

- L. L. Altgilbers, Explosive pulsed power: An enabling technology. Acta Phys. Pol. A 115, 1041 (2009).
- 2. L. L. Altgilbers, B. L. Freeman, Explosive pulsed power (Imperial College Press, 2011).
- X.-Z. Lu, J. M. Rondinelli, Epitaxial-strain-induced polar-to-nonpolar transitions in layered oxides. Nature Mater. 15, 951–955 (2016).
- Z. Gao, W. Peng, B. Chen, S. A. T. Redfern, K. Wang, B. Chu, Q. He, Y. Sun, X. Chen, H. Nie, W. Deng, L. Zhang, H. He, G. Wang, X. Dong, Giant power output in lead-free ferroelectrics by shock-induced phase transition. *Phys. Rev. Mater.* 3, 035401 (2019).
- H. Lu, C.-W. Bark, D. E. de los Ojos, J. Alcala, C. B. Eom, G. Catala, A. Gruverman, Mechanic writing of ferroelectric polarization. Science 336, 59–61 (2012).
- J. Wang, B. Wylie-van Eerd, T. Sluka, C. Sandu, M. Cantoni, X.-K. Wei, A. Kvasov,
 L. J. McGilly, P. Geneiner, B. Dkhil, A. Tagantsev, J. Trodahl, N. Setter, Negative-pressure-induced enhancement in a freestanding ferroelectric. *Nat. Mater.* 14, 985–990 (2015).
- K. Cordero-Edward, N. Domingo, A. Abdollahi, J. Sort, G. Catalan, Ferroelectrics as smart mechanical materials. Adv. Mater. 29, 1702210 (2017).
- A. R. Damodaran, S. Pandya, J. C. Agar, Y. Cao, R. K. Vasudevan, R. Xu, S. Saremi, Q. Li, J. Kim, M. R. McCarter, L. R. Dedon, T. Angsten, N. Balke, S. Jesse, M. Asta, S. V. Kalinin, L. W. Martin, Three-state ferroelastic switching and large electromechanical responses in PbTiO₃ thin films. *Adv. Mater.* 29, 1702069 (2017).
- S. I. Shkuratov, J. Baird, V. G. Antipov, E. F. Talantsev, J. B. Chase, W. Hackenberger, J. Luo, H. R. Jo, C. S. Lynch, Ultrahigh energy density harvested from domain-engineered relaxor ferroelectric single crystals under high strain rate loading. Sci. Rep. 7, 46758 (2017).

- M. Avdeev, J. D. Jorgensen, S. Short, G. A. Samara, E. L. Venturini, P. Yang, B. Morosin, Pressure-induced ferroelectric to antiferroelectric phase transition in Pb_{0.99}(Zr_{0.95}Ti_{0.05})_{0.98}Nb_{0.02}O₃. Phys. Rev. B 73, 064105 (2006).
- S. Patel, A. Chauhan, R. Vaish, C. S. Lynch, Large barocaloric effect and pressure-mediated electrocaloric effect in Pb_{0.99}Nb_{0.02}(Zr_{0.95}Ti_{0.05})_{0.98}O₃ ceramics. J. Am. Ceram. Soc. 100, 4902–4911 (2017).
- H. Nie, Y. Yu, Y. Liu, H. He, G. Wang, X. Dong, Enhanced shock performance by disperse porous structure: A case study in PZT95/5 ferroelectric ceramics. J. Am. Ceram. Soc. 100, 5693–5699 (2017).
- A. Chauhan, S. Patel, S. Wang, N. Novak, B.-X. Xu, P. Lv, R. Vaish, C. S. Lynch, Enhanced performance of ferroelectric materials under hydrostatic pressure. *J. Appl. Phys.* 122, 224105 (2017).
- W. D. Dong, J. C. Valadez, J. A. Gallagher, H. R. Jo, R. Sahul, W. Hackenberger, C. S. Lynch, Pressure, temperature, and electric field dependence of phase transformations in niobium modified 95/5 lead zirconate titanate. *J. Appl. Phys.* 117, 244104 (2015).
- D. Fu, M. Endo, H. Taniguchi, T. Taniyama, M. Itoh, Ag Nb O₃: A lead-free material with large polarization and electromechanical response. Appl. Phys. Lett. 90, 252907 (2007).
- Y. Tian, L. Jin, H. Zhang, Z. Xu, X. Wei, E. D. Politova, S. Y. Stefanovich, N. V. Tarakina,
 I. Abrahamsc, H. Yan, High energy density in silver niobate ceramics. *J. Mater. Chem. A* 4, 17279–17287 (2016).
- L. Zhao, Q. Liu, J. Gao, S. Zhang, J.-F. Li, Lead-free antiferroelectric silver niobate tantalate with high energy storage performance. Adv. Mater. 29, 1701824 (2017).
- X. He, C. Chen, C. Li, H. Zeng, Z. Yi, Ferroelectric, photoelectric, and photovoltaic performance of silver niobate ceramics. Adv. Func. Mater. 29, 1900918 (2019).
- T. T. A. Lummen, J. Leung, A. Kumar, X. Wu, Y. Ren, B. K. VanLeeuwen, R. C. Haislmaier, M. Holt, K. Lai, S. V. Kalinin, V. Gopalan, Emergent low-symmetry phases and large property enhancements in ferroelectric KNbO₃ bulk crystals. *Adv. Mater.* 29, 1700530 (2017).
- D. Fu, M. Itoh, S.-Y. Koshihara, Dielectric, ferroelectric, and piezoelectric behaviors of AgNbO₃–KNbO₃ solid solution. *J. Appl. Phys.* 106, 104104 (2009).
- S. I. Shkuratov, J. Baird, V. G. Antipov, E. F. Talantsev, H. R. Jo, J. C. Valadez, C. S. Lynch, Depolarization mechanisms of PbZr_{0.52}Ti_{0.48}O₃ and PbZr_{0.95}Ti_{0.05}O₃ poled ferroelectrics under high strain rate loading. *Appl. Phys. Lett.* **104**, 212901 (2014).
- H. Jo, C. Lynch, Effect of composition on the pressure-driven ferroelectric to antiferroelectric phase transformation behavior of (Pb_{0.97}La_{0.02})(Zr_{1-x-y}Sn_xTi_y)O₃ ceramics. *J. Appl. Phys.* **116**, 074107 (2014).
- S. I. Shkuratov, J. Baird, V. G. Antipov, W. Hackenberger, J. Luo, S. Zhang, C. S. Lynch, J. B. Chase, H. R. Jo, C. C. Roberts, Complete stress-induced depolarization of relaxor ferroelectric crystals without transition through a non-polar phase. *Appl. Phys. Lett.* 112, 122903 (2018).
- J. Wang, G. Wang, X. Chen, X. Dong, H. Nie, F. Cao, S. Guo, H. He, High room-temperature pyroelectric response of MgO-modified Pb_{0.99}(Zr_{0.95}Ti_{0.05})_{0.98}Nb_{0.02}O₃ ceramics. *Infrared Phys. Tech.* 61, 325–329 (2013).
- P. M. Woodward, Octahedral Tilting in Perovskites. I. Geometrical Considerations. Acta Crystallogr. B 53, 32–43 (1997).
- M. Yashima, S. Matsuyama, R. Sano, M. Itoh, K. Tsuda, D. Fu, Structure of ferroelectric silver niobate AgNbO₃. Chem. Mat. 23, 1643–1645 (2011).
- Z. Liu, T. Lu, J. Ye, G. Wang, X. Dong, R. Withers, Y. Liu, Antiferroelectrics for energy storage applications: A review. Adv. Mater. Tech. 3, 1800111 (2018).
- I. Levin, V. Krayzman, J. C. Woicik, J. Karapetrova, T. Proffen, M. G. Tucker, I. M. Reaney, Structural changes underlying the diffuse dielectric response in AgNbO₃. Phys. Rev. B 79, 104113 (2009)
- T. Lu, Y. Tian, A. Studer, N. Narayanan, Q. Li, R. Withers, L. Jin, Y. Mendez-González, A. Peláiz-Barranco, D. Yu, G. J. McIntyre, Z. Xu, X. Wei, H. Yan, Y. Liu, Symmetry-mode analysis for intuitive observation of structure-property relationships in the lead-free antiferroelectric (1-x)AqNbO₃-xLiTaO₃. IUCrJ 6, 740–750 (2019).
- B. J. Campbell, H. T. Stokes, D. E. Tanner, D. M. Hatch, ISODISPLACE: A web-based tool for exploring structural distortions. J. Appl. Cryst. 39, 607–614 (2006).
- L. Katz, H. D. Megaw, The structure of potassium niobate at room temperature: The solution of a pseudosymmetric structure by Fourier methods. *Acta Cryst.* 22, 639–648 (1967).
- K. E. Johnston, C. C. Tang, J. E. Parker, K. S. Knight, P. Lightfoot, S. E. Ashbrook, The polar phase of NaNbO₃: A combined study by powder diffraction, solid-state NMR, and first-principles calculations. *J. Am. Chem. Soc.* 132, 8732–8746 (2010).
- Y. Liu, R. L. Withers, X. Wei, J. D. F. Gerald, Structured diffuse scattering and polar nano-regions in the Ba(Ti_{1-x}Sn_x)O₃ relaxor ferroelectric system. *J. Solid. Stat. Chem.* 180, 858–865 (2007).
- 34. R. Comes, M. Lambert, A. Guinier, The chain structure of BaTiO₃ and KNbO₃. *Solid Stat. Comm.* **6**, 715–719 (1968).
- F. Xue, L. Liang, Y. Gu, I. Takeuchi, S. V. Kalinin, L.-Q. Chen, Composition- and pressureinduced ferroelectric to antiferroelectric phase transitions in Sm-doped BiFeO₃ system. *Appl. Phys. Lett.* **106**, 012903 (2015).

SCIENCE ADVANCES | RESEARCH ARTICLE

- C. Xu, Z. Fu, Z. Liu, L. Wang, S. Yan, X. Chen, F. Cao, X. Dong, G. Wang, La/Mn Co-doped AgNbO₃ lead-free antiferroelectric ceramics with large energy density and power density. ACS Sust. Chem. Eng. 6, 16151–16159 (2018).
- H. Pohlmann, J.-J. Wang, B. Wang, L.-Q. Chen, A thermodynamic potential and the temperature-composition phase diagram for single-crystalline K_{1-x}Na_xNbO₃ (0<x<0.5). Appl. Phys. Lett. 110, 102906 (2017).

Acknowledgments

Funding: Z.L., H.N., G.W., and X.D. were supported by National Natural Science Foundation of China (NSFC) (no. 61475176), Chinese Academy of Sciences Research Equipment Development Project (no. YZ201332), and Youth Innovation Promotion Association, CAS. Z.L., T.L., N.N., and Y.L. were supported by the Australian Research Council (ARC) in terms of Discovery Project (DP160104780, DP190100295, and DP200100159). Z.L. also thanks the support from the Shanghai Sailing Program (no. 17YF1429700). L.C. was supported by the U.S. National Science Foundation under grant number DMR-1744213. F.X. was supported by the U.S. National Science Foundation under DMREF grant DMR 1629270. The authors also thank the Australian Nuclear Science and Technology Organisation for support in the form of beam time. **Author contributions:** Z.L., Y.L., and G.W. conceived and supervised the project. Z.L. prepared the

samples and measured the properties. H.N. performed the discharging experiments. T.L., Z.L., R.W., A.S., N.N., and Y.L. collected and analyzed the NDPs. T.L., R.W., Z.L., and F.K. carried out the transmission electron microscopy analysis. F.X. and L.C. performed the calculations. Z.L. wrote the paper with contributions from T.L. and F.X. All authors jointly performed data analysis and interpretation and the modification of the manuscript. **Competing interests**: The authors declare that they have no competing interests. **Data and materials availability**: All data needed to evaluate the conclusions in the paper are present in the paper and/or the Supplementary Materials. Additional data related to this paper may be requested from the authors.

Submitted 29 October 2019 Accepted 18 March 2020 Published 20 May 2020 10.1126/sciadv.aba0367

Citation: Z. Liu, T. Lu, F. Xue, H. Nie, R. Withers, A. Studer, F. Kremer, N. Narayanan, X. Dong, D. Yu, L. Chen, Y. Liu, G. Wang, Lead-free (Ag,K)NbO₃ materials for high-performance explosive energy conversion. *Sci. Adv.* **6**, eaba0367 (2020).



Lead-free (Ag,K)NbO₃ materials for high-performance explosive energy conversion

Zhen Liu, Teng Lu, Fei Xue, Hengchang Nie, Ray Withers, Andrew Studer, Felipe Kremer, Narendirakumar Narayanan, Xianlin Dong, Dehong Yu, Longqing Chen, Yun Liu and Genshui Wang

Sci Adv **6** (21), eaba0367. DOI: 10.1126/sciadv.aba0367

ARTICLE TOOLS http://advances.sciencemag.org/content/6/21/eaba0367

SUPPLEMENTARY http://advances.sciencemag.org/content/suppl/2020/05/18/6.21.eaba0367.DC1 MATERIALS

REFERENCES This article cites 36 articles, 1 of which you can access for free

http://advances.sciencemag.org/content/6/21/eaba0367#BIBL

PERMISSIONS http://www.sciencemag.org/help/reprints-and-permissions

Use of this article is subject to the Terms of Service